Journal of Non-Newtonian Fluid Mechanics 334 (2024) 105328

Contents lists available at ScienceDirect

Journal of Non-Newtonian Fluid Mechanics

journal homepage: www.elsevier.com/locate/jnnfm

Full length article

Stokes layers in complex fluids

D.R. Hewitt [a], N.J. Balmforth [b,*]

[a] Department of Applied Mathematics and Theoretical Physics, University of Cambridge, Wilberforce Road, Cambridge CB3 0WA, UK
[b] Department of Mathematics, University of British Columbia, Vancouver, BC, V6T 1Z2, Canada

ARTICLE INFO

Keywords:
Stokes layers
Elasto-viscoplastic fluids
Thixotropy
Discontinuous shear thickening

ABSTRACT

Stokes's second problem is reconsidered for three models of complex fluids: an elasto-viscoplastic fluid, a thixotropic viscoplastic fluid and a discontinuously shear-thickening fluid. In each case, the Stokes-layer dynamics is interrogated with a view to examining the signatures of the detailed rheology. Significant deformations are possible below the yield stress for elasto-viscoplastic fluids as a result of the excitation of elastic waves, particularly near resonances. Thixotropic fluids with viscosity bifurcations layer internally, but surface-speed signatures mostly appear similar to those for simple yield-stress fluids. Stokes-layer oscillations of discontinuous shear thickening fluids can prompt abrupt increases in viscosity, introducing sudden jumps in surface speed. Pre-existing experimental results for layers of kaolin slurries in a motorized, oscillating tray are reconsidered and compared with the results for elasto-viscoplastic and thixotropic fluids.

1. Introduction

In Stokes's second problem, a wall adjacent to a viscous fluid is oscillated back and forth to drive fluid motion; the "Stokes length" characterizes the thickness of the region affected by the oscillating wall. Without lateral side walls, flow remains one-dimensional, a simplification that has motivated a number of previous articles in which the problem was reconsidered for non-Newtonian fluids, partly with the aim of rheological inference (*e.g.* [1–5]). The purpose of the present article is to continue in this vein and consider Stokes's second problem for three other models of complex fluids: an elasto-viscoplastic fluid [6], a thixotropic fluid [7], and a discontinuously shear-thickening fluid [8].

Rheological models that advance beyond traditional ideal viscoelastic or viscoplastic formulations, such as the three considered here, are increasingly prevalent in the modelling of complex fluids. Given the complexity of these constitutive models, it can be difficult to decipher the impact or interaction between different features of the rheology in these models, particularly if the flow is itself already somewhat convoluted. The aim of this work, therefore, is to focus on a canonical, and mathematically simple, fluid-mechanical problem, and to draw out and interpret the impact of different rheological features in this setting. Specifically, we will find that all three rheological models enrich the dynamics of the Stokes-layer problem, whilst retaining its spatial simplicity.

Our exploration of a elasto-viscoplastic fluid model follows directly on from the theoretical analysis presented in [2]: by introducing elastic effects using the model proposed by Saramito [6], we gauge how elastic recoil may impact the viscoplastic response of a fluid layer to oscillatory forcing. Elasticity has previously been reported to be important in related oscillatory flow problems for viscoplastic fluids [9–11], although it was discounted in experiments with kaolin slurries also reported by Balmforth et al. [2]. In fact, Balmforth et al. [2] attributed discrepancies between theory and the kaolin slurry experiments to the presence of thixotropy in that material, partly motivating our study of thixotropic Stokes layers. We revisit Balmforth et al.'s conclusions later in the present study, armed with insights gained from the current theoretical analysis.

The third model fluid we consider is that of a discontinuously shear thickening material [8]. This type of material provides an interesting counterpoint to the other two fluid models in that it may abruptly jam up at high shear rates, rather than plugging up at low shear rates. For our analysis of the Stokes's problem, we use a modification of the model proposed by Wyart & Cates [12], that further allows for time-dependent relaxation of the microstructural changes taking place under an evolving shear rate [13–15].

2. Formulation

Consider a layer of complex fluid described by the Cartesian coordinates, $(\tilde{x}, \tilde{y})$, that is supported by a rigid plane wall which undergoes oscillatory motion along its length. We orientate the plane with the $\tilde{x}$-axis, so that $\tilde{y} = 0$ corresponds to the moving wall, and assume that the

* Corresponding author.
E-mail address: njb@math.ubc.ca (N.J. Balmforth).

https://doi.org/10.1016/j.jnnfm.2024.105328
Received 5 August 2024; Received in revised form 23 September 2024; Accepted 24 September 2024
Available online 3 October 2024
0377-0257/

driven flow remains one-dimensional with velocity $(\tilde{u}(\tilde{y},\tilde{t}),0)$ at time $\tilde{t}$. For a sinsoidal motion of the wall, we set

$$\tilde{u}(0,\tilde{t}) = -\mathcal{U}\cos\omega\tilde{t}, \tag{1}$$

assuming a no-slip condition always holds, where $\mathcal{U}$ and ω are controllable parameters of the problem.

In the absence of any dependence on $\tilde{x}$, the momentum equation for the fluid layer reduces to

$$\rho\frac{\partial\tilde{u}}{\partial\tilde{t}} = \frac{\partial\tilde{\tau}_{XY}}{\partial\tilde{y}}, \tag{2}$$

where $\tilde{\tau}_{XY}$ is the shear stress, which is related to the shear rate

$$\tilde{\dot{\gamma}}_{XY} = \frac{\partial\tilde{u}}{\partial\tilde{y}}, \tag{3}$$

by a suitable constitutive law. Below, we explore three versions of this law, suitable for elasto-viscoplastic, thixotropic and discontinuously shear-thickening fluids. Each of these laws possesses a characteristic viscosity constant, μ_O.

At the top of the fluid layer, $\tilde{y} = \mathcal{H}$, we consider two possible boundary conditions: either no-slip if there is another, stationary wall there, so that $\tilde{u}(\tilde{y}=\mathcal{H})=0$; or a stress-free condition $\tilde{\tau}_{XY}(\tilde{y}=\mathcal{H})=0$ if there is a free surface. Note that, given (2), the first of these conditions implies $\partial\tilde{\tau}_{XY}/\partial\tilde{y}=0$ at $\tilde{y}=\mathcal{H}$.

To remove distracting dimensional constants from the equations, we introduce the dimensionless variables,

$$\tilde{t} = \omega^{-1}t, \quad \tilde{y} = \mathcal{L}y, \quad \tilde{u} = \mathcal{U}\,u(y,t),$$

$$\tilde{\tau}_{XY} = \rho\omega\mathcal{U}\mathcal{L}\,\tau_{XY}(y,t), \quad \tilde{\dot{\gamma}}_{XY} = \frac{\mathcal{U}}{\mathcal{L}}\dot{\gamma}(y,t), \tag{4}$$

where

$$\dot{\gamma}(y,t) = \frac{\partial u}{\partial y} \tag{5}$$

is the dimensionless shear rate and

$$\mathcal{L} = \sqrt{\frac{\mu_O}{\rho\omega}} \tag{6}$$

represents the Stokes length for a Newtonian fluid with viscosity μ_O. The momentum equation (2) then becomes

$$\frac{\partial u}{\partial t} = \frac{\partial\tau_{XY}}{\partial y} \tag{7}$$

and the bottom boundary condition is

$$\frac{\partial\tau_{XY}}{\partial y} = \sin t \quad \text{at} \quad y=0. \tag{8}$$

The two possible upper boundary conditions are

$$\frac{\partial\tau_{XY}}{\partial y} = 0 \quad \text{or} \quad \tau_{XY}=0, \quad \text{at} \quad y = H \equiv \frac{\mathcal{H}}{\mathcal{L}}. \tag{9}$$

The initial conditions depend partly on which of the constitutive laws is employed. Practically, we may differentiate the momentum equation with respect to y to arrive at an evolution equation for the shear rate, demanding an initial condition for $\dot{\gamma}(y,0)$. For a no-slip upper wall, $u(H,t)=0$, this initial condition must satisfy an additional constraint because

$$\int_0^H \dot{\gamma}(y,0)\,\mathrm{d}y = [u(H,t)+\cos t]_{t=0} = 1, \tag{10}$$

which leads us to choose

$$\dot{\gamma}(y,0) = \frac{1}{H}, \tag{11}$$

corresponding to constant initial shear. For a stress-free upper surface, we need not adopt this condition and take instead $\dot{\gamma}(y,0)=0$. Neither choice is particularly significant as we are more interested in the periodic states reached after relatively short transients. However, in the case of the Bingham model, a special case of the elastic-viscoplastic model considered next, it does constrain the initial shear stress. We outline the remaining initial conditions later, once we establish the forms of the constitutive laws that we employ. Some details of the numerical schemes we use to solve each of the models are given in Appendix A.

3. Elasto-viscoplastic fluid

For an elasto-viscoplastic fluid, we adopt a one-dimensional version of Saramito's model, which sets the (dimensional) shear stress equal to a sum of polymer and solvent components:

$$\tilde{\tau}_{XY} = \tilde{\tau}(\tilde{y},\tilde{t}) + \beta\mu_O\dot{\gamma}(\tilde{y},\tilde{t}), \tag{12}$$

where $\tilde{\tau}(y,t)$ is the polymer shear stress, and $\beta\mu_O$ is the solvent viscosity (so that β represents a viscosity ratio). The polymer stress satisfies the dimensional equation [6]

$$\frac{1}{\lambda}\frac{\partial\tilde{\tau}}{\partial\tilde{t}} + \max(0,|\tilde{\tau}|-\tau_P)\,\mathrm{sgn}(\tau) = \mu_O\frac{\partial\tilde{u}}{\partial\tilde{y}}, \tag{13}$$

where λ is a relaxation rate. Note that Saramito's model is normally posed with an upper convected derivative on the stress tensor, which can activate nontrivial extensional stress components in addition to the shear stress (*cf.* [1]). The presence of such normal stresses (and their differences) implies that the yield condition, which is based on a von Mises criterion in Saramito's model, should encode more than just the shear stress. In (13), however, we opted for simplicity and stated the yield condition only in terms of τ_{XY}, which avoids the need to include additional evolution equations for the normal stresses.

With our characteristic scalings, we now arrive at the model dimensionless system,

$$\begin{aligned} &\dot{\gamma}_t = \tau_{yy} + \beta\dot{\gamma}_{yy}, \\ &\mathrm{De}\,\tau_t + \max(0,|\tau|-\mathrm{Bi})\,\mathrm{sgn}(\tau) = \dot{\gamma} \equiv u_y, \end{aligned} \tag{14}$$

where we have used y and t subscripts as shorthand for partial derivatives. The two new dimensionless parameters are the Bingham and Deborah numbers,

$$\mathrm{Bi} = \frac{\tau_P\mathcal{L}}{\mu_O\mathcal{U}} \equiv \frac{\tau_P}{\rho\omega\mathcal{L}\mathcal{U}} \quad \& \quad \mathrm{De} = \frac{\omega}{\lambda}, \tag{15}$$

which characterize, respectively, the relative importance of plastic and viscous forces, and the elastic response time relative to the timescale of the forcing from the wall. As mentioned above, the initial conditions are either

$$\dot{\gamma}(y,0) = H^{-1} \quad \& \quad \tau(y,0) = H^{-1} + \mathrm{Bi}, \tag{16}$$

for a no-slip upper wall, or $\dot{\gamma}(y,0)=\tau(y,0)=0$ for a stress-free surface.

3.1. Sample solutions

Sample solutions for different values of the depth H are shown in Figs. 1–3 for fixed $\mathrm{Bi}=1$ and $\beta=0$. Each figure contains solutions for varying De, illustrating the impact of elasticity. Consider first the Bingham solutions with $\mathrm{De}=0$, which are similar to those provided earlier in [2,5]. For the Bingham number Bi used in these figures, the fluid mostly yields near the base but the cycle is punctuated by briefer intervals during which the fluid freezes onto the moving wall. The resulting plugs subsequently ascend through the layer. When the top surface is free, these plugs expand, and the yield surfaces eventually meet to leave the overlying fluid permanently plugged. Where the yield surfaces meet and a yielded region disappears, there is an abrupt switch in shear stress. For the shallowest depth H shown here (Fig. 1), the plug occupies the entire fluid depth during part of the cycle, pinning the surface speed to the base speed; with larger depths (Figs. 2 and 3) a yielded region always intervenes somewhere within the fluid layer rendering the surface speed into a sawtooth shape.

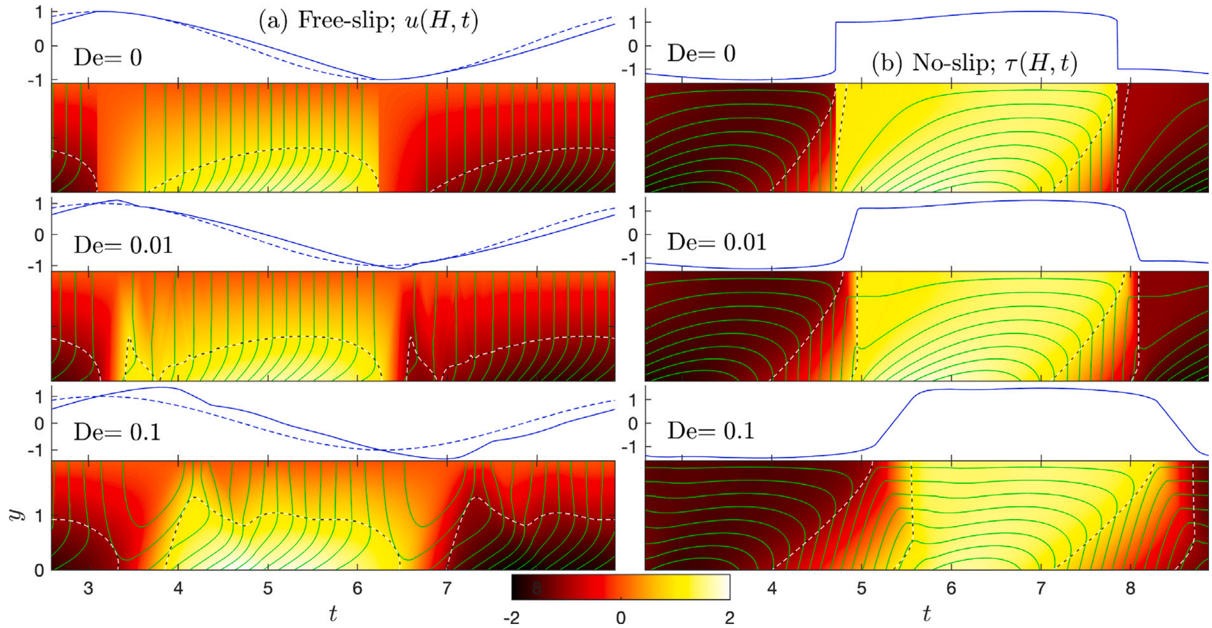

Fig. 1. Elasto-viscoplastic Stokes layers with Bi = 1, $\beta = 0$, $H = 2$, for (a) a free-slip upper surface, and (b) a no-slip top surface. Solutions for three Deborah numbers are displayed, De $= 0, 0.01, 0.1$, increasing from top (De $= 0$) to bottom. Shown are time series of (a) $u(H,t)$ (solid) and $u(0,t)$ (dashed), and (b) $\tau(H,t)$; density maps below show $\tau(y,t)$. The dashed lines show the yield surfaces and the green lines indicate contours of constant speed.

.

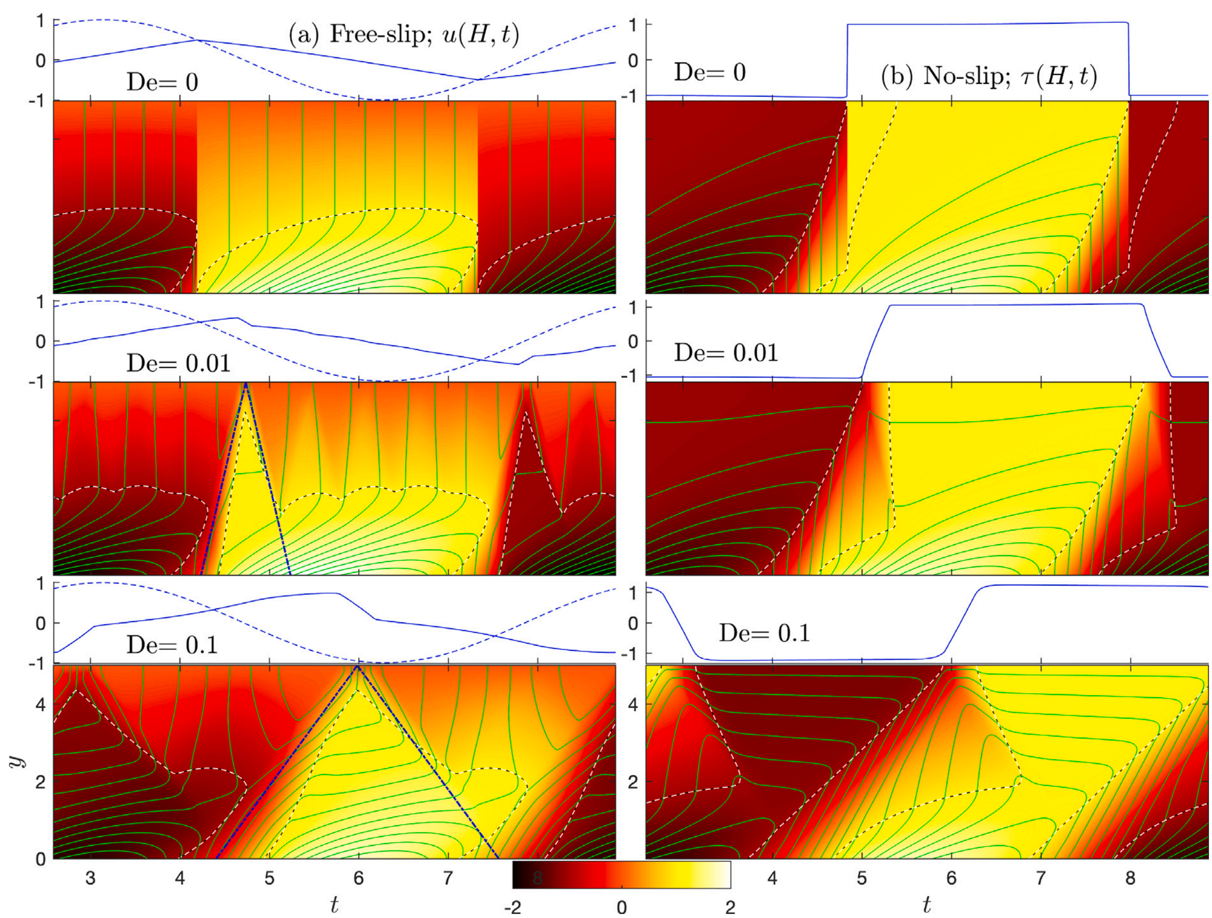

Fig. 2. As for Fig. 1, but for $H = 5$. The thicker (blue, dot-dashed) lines plotted on the density plots in the left column indicate local elastic ray paths. .

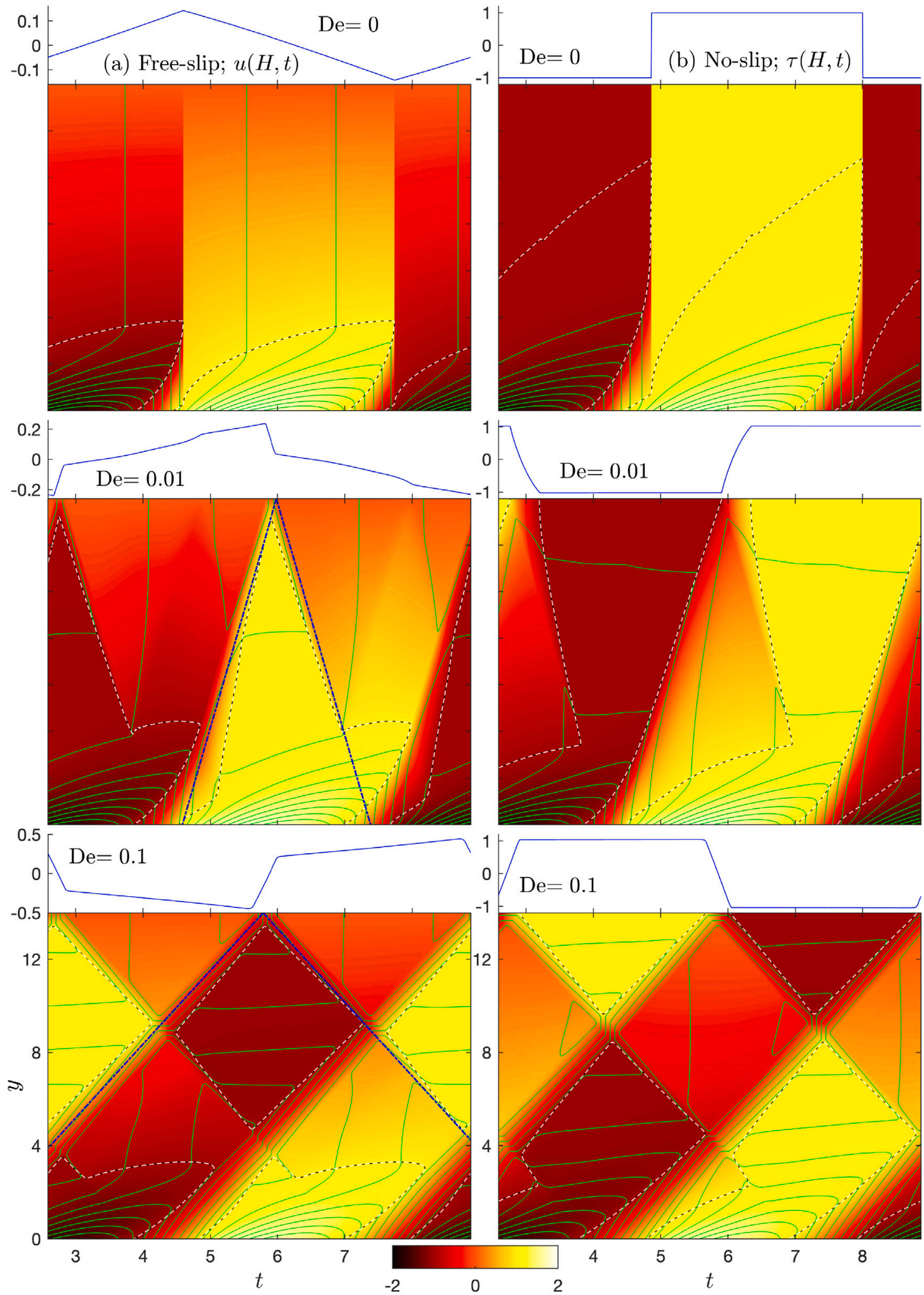

Fig. 3. As for Figs. 1 and 2, but for $H = 14$; $u(0,t)$ is not plotted in (a). Again, the thicker (blue, dot-dashed) lines plotted on the density plots in the left column indicate local elastic ray paths.

For a no-slip upper wall, the plugs can either narrow or expand as they ascend through the layer; for the smaller two depths, the yielded regions reach the surface, but for the largest depth these regions again disappear to leave a plug at the top. The disappearance of a yielded region (either within the layer or at the top wall) again prompts a jump in stress. As a result of these switches, the top shear stress resembles a square-wave.

For finite relaxation times, De > 0, the structure of the solutions becomes somewhat different, although in all the cases, the solutions share the same alternation between yielding and freezing at the base.

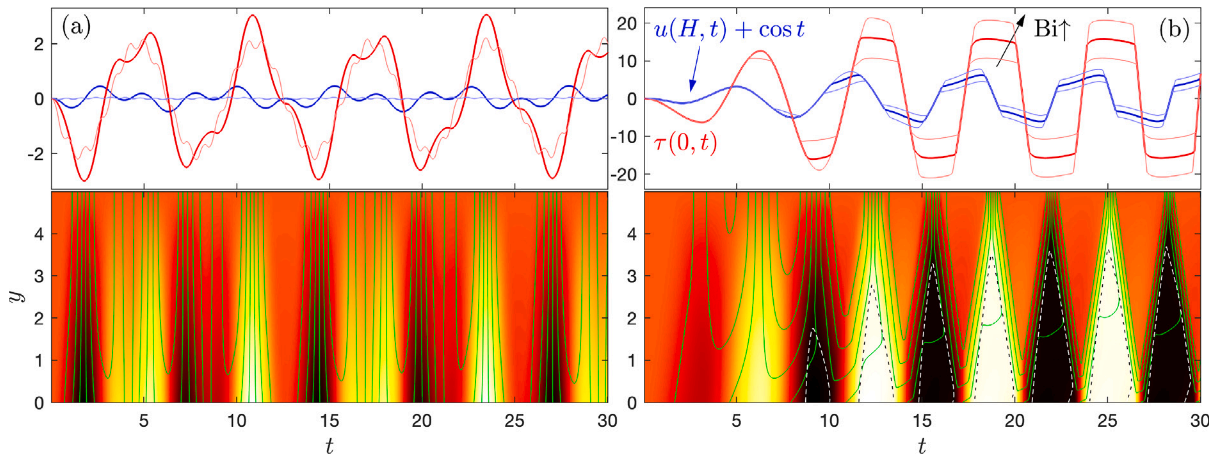

Fig. 4. Elasto-viscoplastic layers with a stress-free surface for (a) $(H, \mathrm{Bi}) = (2, 4)$ and (b) $(H, \mathrm{Bi}) = (5, 15)$; $(\mathrm{De}, \beta) = (0.1, 0)$. Upper panels show $u(H,t) + \cos t$ (blue) and $\tau(0,t)$ (red); lower panels display density plots of $\tau(y,t)$ with superposed constant-speed contours (green). In (a), fluid remains unyielded throughout; for (b), resonantly driven elastic waves prompt yielding within the yield surfaces shown by dashed lines. The lighter lines in (a) show a second solution with De = 0.01. The lighter lines in (b) show two more solutions with Bi = 10 and 20.

A key difference with the Bingham case is that stress signals begin to translate in space over the plugged regions when De > 0. To understand this feature, we combine the two equations in (14) into the nonlinearly damped wave equation,

$$\mathrm{De}\,\tau_{tt} + \tau_t \Theta(|\tau| - \mathrm{Bi}) = \tau_{yy}, \tag{17}$$

where $\Theta(x)$ denotes the Heaviside step function. The damping switches off when τ falls below the yield stress, leaving a linear wave equation for the shear stress with a wave speed of $\mathrm{De}^{-\frac{1}{2}}$.

The elastic (first) term in (17) implies that the sudden switches in stress which arise for the Bingham model must become smoothed by elasticity (see also [10,11]). In some cases, the resulting sudden, but smoothed, changes in stress excite a translating elastic response that follows the ray paths $y \pm \mathrm{De}^{-\frac{1}{2}} t = constant$ (see the blue lines drawn in Figs. 2 and 3), leading to a sawtooth-like pattern in the space–time plots of the stress field. For the shallower layers in Figs. 1 and 2, these elastic disturbances (which are similar to flow structures reported in [11]) are damped rather abruptly once stresses return to levels exceeding Bi and the fluid yields again. For the deeper layers in Fig. 3, the transmitted stresses only weakly yield the upper regions, generating checkerboard patterns on the space–time plots. The surface signals in $u(H,T)$ or $\tau(H,t)$ become shifted and more structured as a result of this dynamics.

Note that in the viscoplastic limit, a free slip upper surface has the feature that the entire layer can remain rigid and unyielded when Bi > H. The fluid layer then oscillates like a rigid solid. For De > 0, however, an elastic deformation still arises, as illustrated by the solution on the left of Fig. 4 with De = 0.1. In this case, the driving by the wall excites elastic oscillations, leading to a multiply periodic surface signal, with an amplitude set by De (*cf.* the second solution included in Fig. 4(a) with De = 0.01). Nevertheless, as illustrated by the contours of constant speed added to the space–time density plot of $\tau(y,t)$ in Fig. 4(b), the layer still oscillates sideways largely as whole.

More dramatic elastic behaviour below the yield stress is also possible. The non-dissipative wave equation that applies when τ fails to breach the yield stress possesses the elastic normal-mode solutions,

$$\tau \propto \cos \omega_n t \cos k_n y, \quad \omega_k = \frac{k_n}{\sqrt{\mathrm{De}}}, \tag{18}$$

with $k_n = (n - \frac{1}{2})\pi/H$ for the free-surface case and $k_n = n\pi/H$ for no-slip. Such modes can be resonantly driven by the motion of the underlying wall, as in viscoelastic Stokes layers [1,3]. If the condition for resonance is met, $\omega_n = 1$, stresses are then expected to grow linearly with time until fluid yields, at which point dissipative viscoplastic deformation can arrest growth.

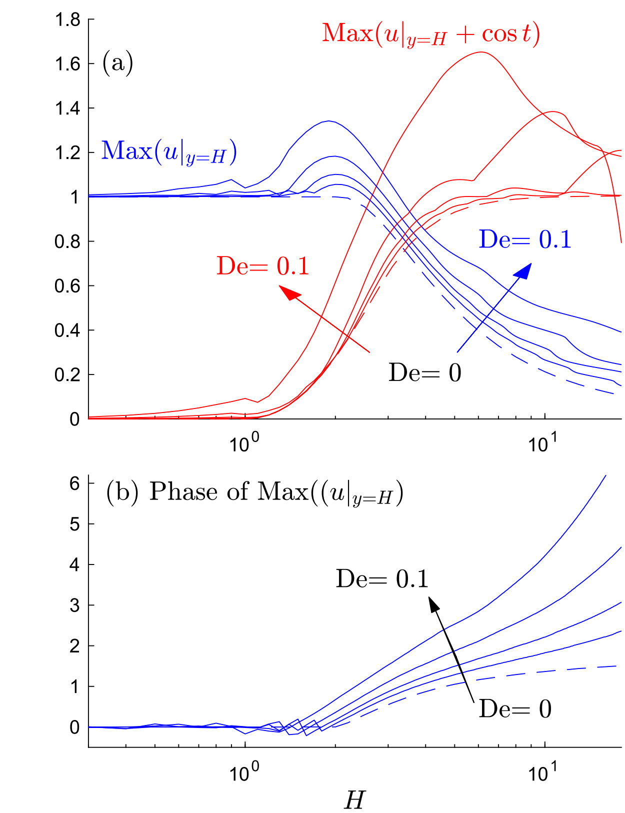

Fig. 5. (a) Maximum surface speed and relative surface speed against H for Bi = 1 and De = 0, 0.00316, 0.01, 0.0316 and 0.1. (b) The phase of the maximum surface speed, relative to the maximum base speed (which occurs at $t = \pi$). The dashed lines shows the results for the Bingham (De = 0) model.

The shallowest layer for which resonance occurs is $H = H_R$, with $H_R = \pi/2\sqrt{\mathrm{De}}$ (free-surface) or $H_R = \pi/\sqrt{\mathrm{De}}$ (no-slip). With De = 0.1 we have $H_R \approx 4.97$ or 9.93. On the right of Fig. 4, we show a free-surface solution displaying near-resonant dynamics, in which the spatio-temporal oscillations in stress and surface speed reach relatively large amplitude.

Fig. 5 displays "response curves" for a layer with a free surface. These curves are plots of the maximum over the final periodic cycle of either the surface speed, $\mathrm{Max}(|u(H,t)|)$, or the relative speed,

$\mathrm{Max}(|u(H,t)+\cos t|)$, for $(\mathrm{Bi},\beta)=(1,0)$ and varying De. For a Bingham fluid, De $=0$, the entire layer remains unyielded for $H<\mathrm{Bi}=1$, and these curves demonstrate no response. For $H>\mathrm{Bi}$, the response develops as indicated by the dashed lines. For finite De, on the other hand, the fluid can deform elastically for $H<\mathrm{Bi}=1$, leading to a finite response that increases with De. The response curves also show broad elevated responses in maximum surface speed for $H>\mathrm{Bi}$, corresponding to the remnants of elastic resonances at $H=H_R$. The phase at which the surface speed achieves its maximum increases with both H and De.

3.2. Shallow or deep layers

For $H\ll 1$ and a no-slip surface, $\dot\gamma$ and τ become independent of y while u becomes linear:

$$u\sim-\left(1-\frac{y}{H}\right)\cos t \tag{19}$$

The dynamics is then all controlled by the constitutive law, which becomes

$$\mathrm{De}\,\tau_t+\max(0,|\tau|-\mathrm{Bi})\,\mathrm{sgn}(\tau)=\frac{\cos t}{H}. \tag{20}$$

The role of the momentum equation is simply to dictate the spatially varying corrections to the solution to (20). In other words, in this limit, variations in space play a minor role and the problem reduces to that for a controlled shear-rate rheometer, as discussed by Saramito [6].

With a free surface, the shallow limit is different, with

$$u\sim-\cos t,\qquad \tau\sim-y\cos t, \tag{21}$$

which ensure that the momentum equation and boundary conditions are satisfied. The constitutive law now determines the spatially varying correction to the leading-order flow speed. This particular limit is less interesting because significant shear and stress are unable to build up against the free surface.

For deep layers, the solution near the lower moving wall becomes insensitive to the fluid depth H and top boundary condition, as illustrated by the shear stresses plotted in Fig. 6(a,b). For a Bingham fluid, this is demanded once the top of the fluid layer becomes plugged throughout the cycle, which implies that the upper boundary becomes irrelevant. The situation is less clear for an elasto-viscoplastic fluid because of the propagation of elastic disturbances to the top surface. However, once those disturbances reflect back down from the top surface they become strongly damped over the lower yielded regions, nullifying their impact. Note that the checkerboard patterns appearing for De >0 in Figs. 3 and 6 indicate that the layer can contain an arbitrarily large number of plugs at a given time for sufficiently large H and De, unlike the Bingham case [2,5].

With a free surface, the large inertia of the upper plug arrests motion for a Bingham fluid. Indeed, as discussed in [2], the surface speed is expected to adopt a sawtooth form with a maximum amplitude of $\frac{1}{2}\pi\mathrm{Bi}H^{-1}$ for a very deep layer; *cf.* Fig. 6(c). This feature does not persist with De >0, however. Instead, the checkerboard generated by propagating elastic waves leads to a square-wave signal in the top shear stress and speed, the latter scaling with the elastic wavespeed $\mathrm{De}^{-1/2}$ (Fig. 6(c)). The surface signal for both stress-free and no-slip upper boundaries becomes delayed by the travel time of the elastic waves, accounted for in Fig. 6(c,d) by plotting $u(H,t)$ and $\tau(H,t)$ against the shifted time, $t-H\sqrt{\mathrm{De}}$.

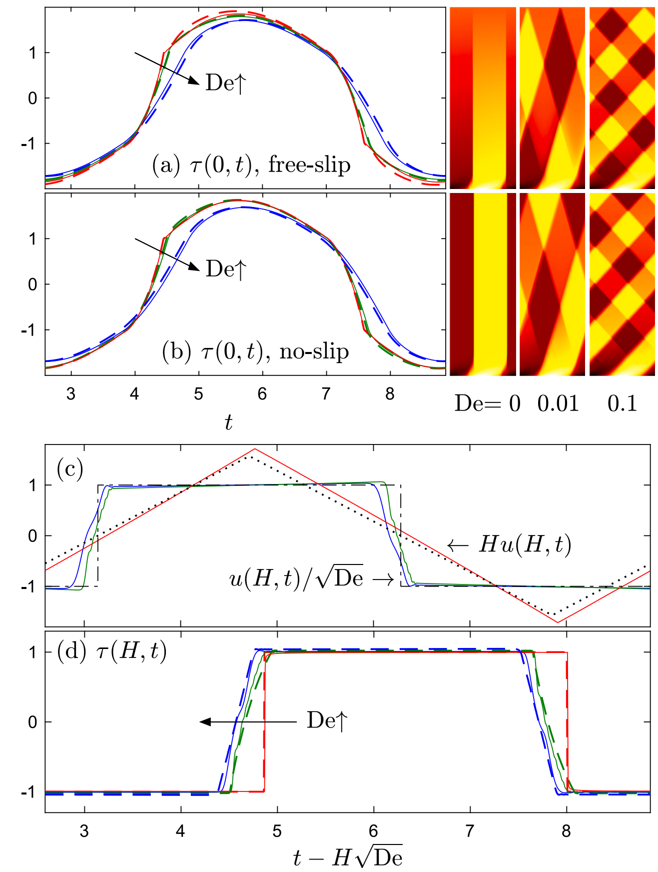

Fig. 6. (a,b) Left-hand panels show the basal shear stresses $\tau(0,t)$ for relatively deep layers ($H\gg 1$) with (a) a free surface, and (b) a no-slip upper wall (Bi $=1$ and $\beta=0$). Solid lines show results for $H=50$; dashed lines reproduce the results for $H=14$ from Fig. 3. The Bingham case is plotted in red, the results for De $=0.01$ in green and those for De $=0.1$ in blue. The right-hand panels show the corresponding space–time density plots of $\tau(y,t)$ for $H=50$. Although the colour scale is not shown for these density plots, it can be inferred from the y–axes of (a,b). Corresponding surface speeds are plotted in (c) for the layer with a free surface; the top shear stress $\tau(H,t)$ is plotted in (d) for the no-slip upper wall. Both signals are plotted against the delayed time $t-H\sqrt{\mathrm{De}}$. In (c), for De $=0$ and $H=50$, the surface speed scaled by depth, $Hu(H,t)$ (red, solid), is compared with a sawtooth wave (dotted; [2]). For De $=(0.01,0.1)$ and $H=50$, the surface speed scaled by the elastic wavespeed, $u(H,t)\sqrt{\mathrm{De}}$ (solid blue and green), is compared against a square wave (dash-dotted).

4. Thixotropic fluid

4.1. Constitutive model

For a thixotropic fluid, we employ the constitutive model,

$$\begin{aligned}&\frac{\partial\Lambda}{\partial\tilde t}=\frac{1-\Lambda}{T}-\alpha\Lambda|\tilde{\dot\gamma}|+K\frac{\partial^2\Lambda}{\partial\tilde y^2},\\ &\tilde\tau=\left[\frac{\tau_p(\Lambda)}{|\tilde{\dot\gamma}|}+\tilde\mu(\Lambda)\right]\tilde{\dot\gamma},\ \text{if } |\tilde\tau|>\tau_p(\Lambda),\\ &\tilde{\dot\gamma}=0\ \text{otherwise},\end{aligned} \tag{22}$$

where $\tau_p(\Lambda)$ and $\tilde\mu(\Lambda)$ are suitable constitutive functions describing the yield stress and viscosity of the material, respectively. This model effectively combines the Bingham law with an evolution equation for an order parameter, $\Lambda(y,t)$, that describes the degree of internal structure [7,16,17]. The order parameter lies in a range $[0,1]$; for $\Lambda=0$, the fluid has no effective microstructure, while it is fully structured when $\Lambda=1$. The evolution equation in (22) contains a restructuring term $(1-\Lambda)/T$ that drives Λ towards the fully structured state, and a destruction term dictated by the local shear rate $|\tilde{\dot\gamma}|$. Restructuring is characterized by a healing timescale T and destruction is parameterized by α. We have also included a diffusive term to account for any spatial structural diffusion, with diffusivity K.

The framework in (22) captures a range of constitutive behaviour. We choose to focus on thixotropic materials with a yield stress, and set

$$\tau_p(\Lambda)=\tau_*\Lambda\quad\&\quad\mu(\Lambda)=\mu_O, \tag{23}$$

where μ_O is again the characteristic viscosity. That is, we adopt a Bingham-like model in which only the yield stress depends on the structure parameter Λ. Overall, while this construction differs slightly from non-viscoplastic thixotropic models (*e.g.* [4]), it is qualitatively similar to numerous others proposed in the literature, producing comparable flow curves in steady, uniform shear [18–21], as discussed in the following subsection.

With the rescalings in (4), we arrive at the model,

$$\begin{aligned} \dot{\gamma}_t &= \tau_{yy}, \\ \dot{\gamma} &= \max(0, |\tau| - \Lambda \mathrm{Bi})\,\mathrm{sgn}(\tau), \\ \mathcal{T}\Lambda_t &= 1 - \Lambda - \Gamma|\dot{\gamma}|\Lambda + \beta\Lambda_{yy} \end{aligned} \tag{24}$$

with

$$\mathcal{T} = \omega T, \quad \mathrm{Bi} = \frac{\tau_* \mathcal{L}}{\mu_o \mathcal{U}}, \quad \Gamma = \frac{\alpha U T}{\mathcal{L}}, \quad \beta = \frac{KT}{\mathcal{L}^2}. \tag{25}$$

The important new parameters here are $\mathcal{T}$, which characterizes how rapidly material rheology adjusts relative to the imposed oscillation period (a thixotropic analogue to the Deborah number of the previous section) and Γ, which compares the rate of destruction to that of aging. The remaining parameter, β, describes the importance of structural diffusion. Our main concern here, however, is the effect of rheological variations through thixotropy, rather than structural diffusion. Indeed, we include the diffusion term in (24) partly to ensure that solutions remain well resolved in space in situations in which sharp variations may appear. We therefore fix $\beta = 3 \times 10^{-5}$ and avoid exploring the effect of varying this parameter.

For brevity, we focus on one set of boundary conditions, a stress-free upper surface, so that

$$\tau_y(0,t) = \sin t \qquad \& \qquad \tau(H,t) = 0. \tag{26}$$

That said, for completeness we provide some illustrative solutions with a no-slip upper boundary in Appendix B. We further adopt no flux conditions on the structure function ($\Lambda_y(0,t) = \Lambda_y(H,t) = 0$), which are required because of the second-order derivative in the diffusion term. In other words, we assume that structure is neither created nor destroyed by interfacial interaction.

As initial conditions, we mostly set $\tau(y,0) = 0$ and $\Lambda(y,0) = 0$, ignoring the transient before the final periodic state. In §4.4, however, we examine such transients more closely and select other initial values for $\Lambda(y,0)$.

4.2. Flow curves

The flow curve for the model follows from considering steady, spatially uniform conditions. In this setting, provided the applied stress τ does not exceed Bi, the fluid can be unsheared, $\dot{\gamma} = 0$, and fully structured, $\Lambda = 1$. Alternatively, for $\dot{\gamma} > 0$, Eq. (24) implies

$$\Lambda = \frac{1}{1 + \Gamma\dot{\gamma}} \quad \& \quad \tau = \dot{\gamma} + \frac{\mathrm{Bi}}{1 + \Gamma\dot{\gamma}}. \tag{27}$$

Such states are illustrated in Fig. 7 and require the applied stress to exceed a certain threshold. For $\Gamma\mathrm{Bi} < 1$, this threshold is the yield stress of the fully structured state, $\tau_{_A} = \mathrm{Bi}$, and the flow curve resembles that for a simple (non-thixotropic) yield-stress fluid. The two lower flow curves in Fig. 7(a) illustrate this situation. If $\Gamma\mathrm{Bi} > 1$, however, the flow curve bends down for a range of shear rates, before reaching a minimum at $(\dot{\gamma}, \tau) = (\dot{\gamma}_{_C}, \tau_{_C})$, and then ascending. Such a minimum in the flow curve at finite shear rate implies an alternative stress threshold given by $\tau = \tau_{_C}$ where

$$\tau_{_C} = \frac{1}{\Gamma}(2\sqrt{\Gamma\mathrm{Bi}} - 1) \qquad \left(\dot{\gamma}_{_C} = \frac{\sqrt{\Gamma\mathrm{Bi}} - 1}{\Gamma}\right). \tag{28}$$

The upper three flow curves in Fig. 7(a) display this second type of behaviour. As illustrated in Fig. 7(b), such flow curves imply excursions along hysteretic loops on first increasing, then decreasing the stress, in the conventional manner of thixotropy. Sudden jumps in shear rate, or viscosity bifurcations, arise at the stresses $\tau = \tau_{_A}$ and $\tau = \tau_{_C}$. One further expects the descending branch of the flow curve, for $\dot{\gamma} < \dot{\gamma}_{_C}$, to be unstable.

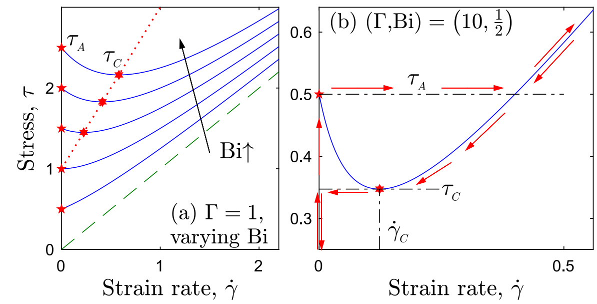

Fig. 7. Steady-state flow curves for (a) $\Gamma = 1$ and varying Bi, and (b) $(\Gamma, \mathrm{Bi}) = \left(10, \frac{1}{2}\right)$, indicating the special stresses $\tau_{_A}$ (stars at $\dot{\gamma} = 0$) and $\tau_{_C}$ (stars and dotted line). The dashed line in (a) corresponds to a viscous fluid with Bi = 0. The arrows in (b) indicate the path of a hysteretic loop taken on first increasing then decreasing the stress, starting from an initially structured state with $\Lambda = 1$.

Note that the flow curves in steady shear are functions of Bi alone when the stress and strain rate are both multiplied by Γ (an indirect consequence of our scaling of the problem). Repeating this scaling for the Stokes problem eliminates the parameter Γ from (24). However, the boundary condition then becomes $\Gamma\tau_y(0,t) = \Gamma \sin t$, indicating that $\Gamma\tau(0,t) = \Gamma H \sin t$ when $\dot{\gamma} = 0$. Therefore, ΓH can also be thought of as a measure of the dimensionless driving stress. Should this stress fail to exceed $\Gamma\tau_{_A} = \Gamma\mathrm{Bi}$, the implication is that the motion of the wall creates insufficient stress to drive deformation in the fluid. That is, the layer remains unyielded, if it is to begin with, furnishing the yield condition, $H < \mathrm{Bi}$, as in the problem for a non-thixotropic (and non-elastic) yield-stress fluid (see [2] and §3.1).

4.3. Thixotropic Stokes layers

Solutions to the Stokes problem for two values of Γ are shown in Figs. 8 and 9. For the cases shown in Fig. 8, there is no hysteresis in the flow curve and the fluid acts like a simple yield-stress fluid in steady-state shear. For sufficiently small relaxation times $\mathcal{T}$ (case (a)), the fluid locally restructures to follow the steady-state flow curve; the upper region remains relatively strongly structured and plug-like regions appear similar to those found for a Bingham fluid. For larger relaxation times (case (b)), the restructuring of the fluid does not take place sufficiently quickly during the cycle to follow the steady flow curve closely.

For yet higher relaxation times (case (c)), the oscillation of the plate becomes too fast to significantly restructure the fluid at all during a single period. Now the cycle-averaged shear rate or stress dictates the local degree of structure and Λ becomes approximately steady, but spatially varying (*cf.* [4]). In this case, discarding diffusion (then dividing (24) by Λ and averaging), we have

$$\Lambda \sim (1 + \Gamma\langle|\dot{\gamma}|\rangle)^{-1}, \tag{29}$$

as seen in Fig. 8(f). The corresponding spatially varying viscosity then controls the dynamics of the fluid layer.

Despite the varying relaxation times and structure functions between the three cases in Fig. 8, the actual differences induced in $u(y,t)$ by the thixotropic evolution is relatively small (see the speed contours plotted in panels (a,b,c)). Indeed, there is minimal discernible impact on the surface velocity field (Fig. 8(d)), which matches that for the non-thixotropic Bingham-like model implied by the flow curve. The space–time pattern of the shear stress $\tau(y,t)$ also remains similar to those for the Bingham model (one can see this by comparing the yield surfaces displayed in Figs. 8 with those for De $= 0$ in Fig. 1(a)).

Fig. 9 presents corresponding examples with parameter settings that lead to a thixotropic hysteresis in steady shear. At low relaxation times (case (a)), local restructuring essentially follows the stable branches of

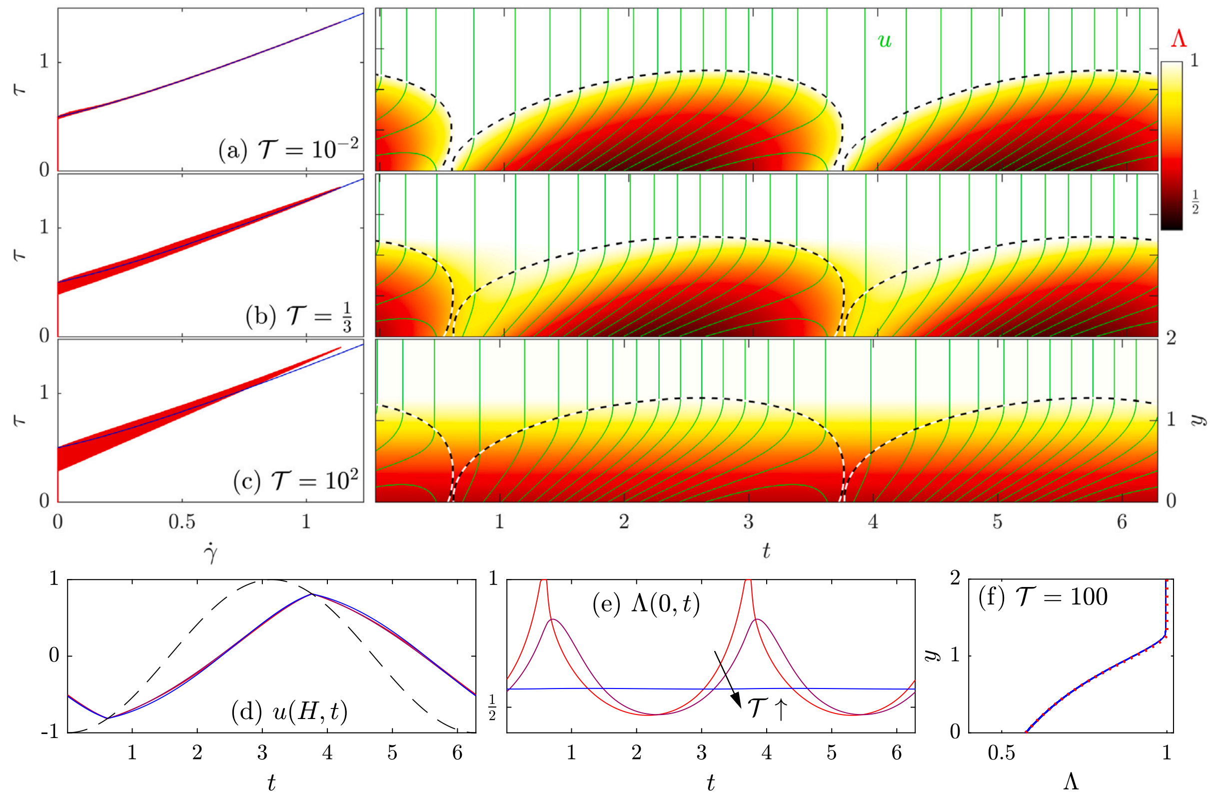

Fig. 8. Steady periodic states for (a) $\mathcal{T} = 10^{-2}$, (b) $\frac{1}{3}$ and (c) 10^2, with $(\mathrm{Bi}, \Gamma, H) = (0.5, 1, 2)$. On the right, structure functions $\Lambda(y,t)$ are shown as a densities over the (y,t)–plane. The dashed contours indicate the yield surfaces, $\tau(y,t) = \pm\Lambda\mathrm{Bi}$, and the green lines are contours of constant speed u. On the left, the (red) points show a scatter plot of $(\dot{\gamma}, \tau)$ along with the steady flow curve (blue). Corresponding time series of (d) surface speed $u(H,t)$ and (e) $\Lambda(0,t)$ are plotted below ($\mathcal{T}$ increasing from red to blue; the dashed line in (d) shows $u(0,t)$). The final panel (f) plots the profile of Λ for $\mathcal{T} = 100$; the red dotted line shows (29).

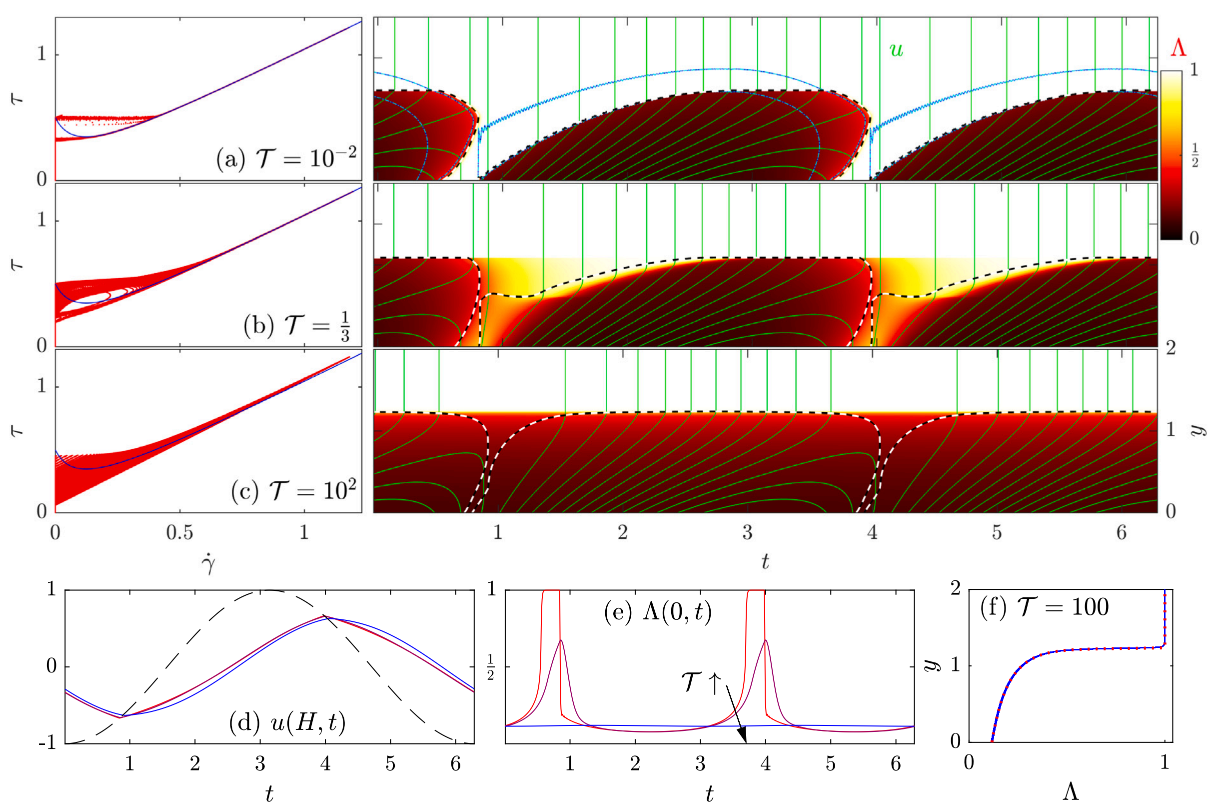

Fig. 9. Solutions as for Fig. 8, but for $\Gamma = 10$. The additional blue speckled contours in (a) show the contours where $\tau(y,t) = \tau_A \equiv \mathrm{Bi}$ and $\tau(y,t) = \tau_c$.

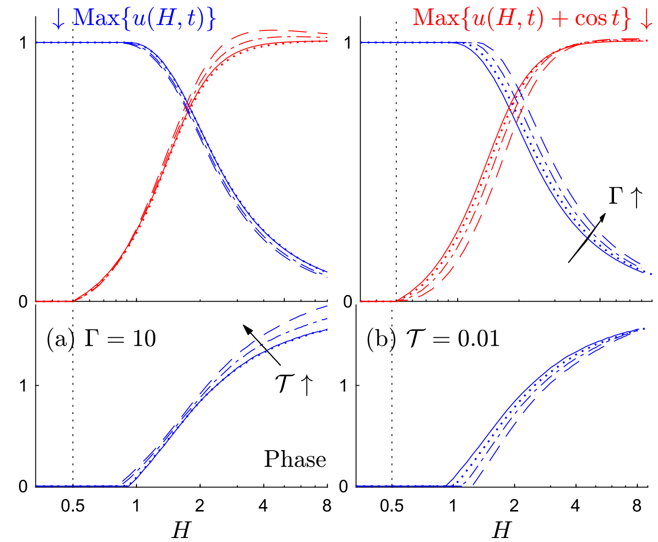

Fig. 10. Maximum surface speed and relative surface speed against H for (a) $\Gamma = 10$ and varying $\mathcal{T}$ (0.01, *solid*; 0.1, *dotted*; 1, *dot-dashed*; 10, *dashed*), and (b) $\mathcal{T} = 0.01$ and varying Γ (1, *solid*; 2.5, *dotted*; 5, *dot-dashed*; 10, *dashed*). The phase of the maximum surface speed relative to the maximum base speed ($t = \pi$) is shown below. In both cases, $\mathrm{Bi} = 0.5$, and the vertical dotted lines indicate the threshold $H = H_{crit} = \mathrm{Bi} = \frac{1}{2}$.

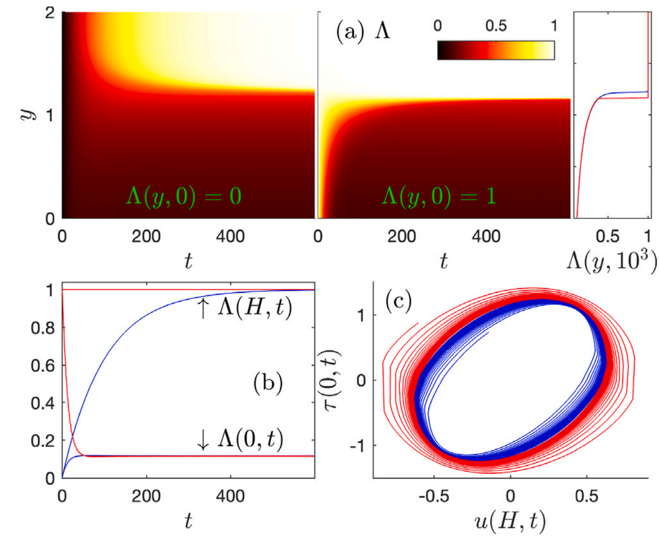

Fig. 11. (a) Density plots of $\Lambda(y,t)$, (b) time series of $\Lambda(0,t)$ and $\Lambda(H,t)$, and (c) phase portraits of $(u(H,t), \tau(0,t))$ after the first cycle; $(\mathcal{T}, \Gamma, H, \mathrm{Bi}) = (100, 10, 2, \frac{1}{2})$. Two solutions are shown, with the first beginning from the unstructured state ($\Lambda(y,0) = 0$; blue in (b,c)), and the second commencing fully structured ($\Lambda(y,0) = 1$; red in (b,c)). On the right of (a), the spatial profiles of the structure function at the later time of $t = 10^3$ are displayed.

the flow curve, with rapid jumps arising at the bifurcations τ_A and τ_C. Note how the yield surface $y = Y(t)$, defined by $|\tau| = \Lambda\mathrm{Bi}$, follows the contour $\tau = \tau_A$ ($\Lambda = 1$) in regions where it advances into fully structured fluid on the left side of each yielded region. The yield surface then jumps over to the contour $\tau = \tau_C$ ($\Lambda = \Lambda_C \equiv 1/\sqrt{\Gamma\mathrm{Bi}}$) on the right of those regions where $y = Y(t)$ retreats into destructured fluid, converting material rapidly back into the fully structured state. Over the jump between these two contours, the yield surface holds a fixed position. Note that the stress contours in Fig. 9(a) feature some relatively fast, small amplitude oscillations. These fine scales are triggered by the sudden destructuring of fluid at the base when the yield condition is met and flow is initiated. A destructuring front then ascends into the overlying structured fluid. However, the front migrates unsteadily, with a decaying oscillation set by the relaxation time $\mathcal{T}$.

For higher $\mathcal{T}$, the relaxation of the microstructure obscures the $\dot{\gamma} - \tau$ plot, although pathways corresponding to the two bifurcations are still evident (case (b)). Once again, for relatively large relaxation times (case (c)), Λ becomes nearly time-independent and given by (29). However, the final state is now layered, with a spatial viscosity bifurcation arising near the midway point. Again we observe that the surface speed is relatively insensitive to $\mathcal{T}$ (Fig. 9d), despite significant spatio-temporal evolution of Λ (panels (a,b,c,e)).

In Fig. 10, we present response curves for the thixotropic model with $\mathrm{Bi} = \frac{1}{2}$ at fixed $\Gamma = 5$ and varying $\mathcal{T}$, or fixed $\mathcal{T} = 0.01$ and varying Γ. Importantly, in none of these examples does the maximum surface speed display a significant enhancement over the maximum speed of the moving wall. This feature contrasts sharply with the predictions shown in Fig. 5 for elasto-viscoplastic Stokes layers, a difference that we return to in Section 6 when discussing previous experimental results.

4.4. Long relaxation

Note that the solutions shown in Figs. 8(c) and 9(c) portray the final, periodic state. However, at such large relaxation times there is a protracted transient from a general initial condition that spans many oscillations of the moving wall (see also [4]). The transients arising from two different initial conditions (completely unstructured, $\Lambda(y,0) = 0$, or fully structured, $\Lambda(y,0) = 1$) are shown in more detail in Fig. 11. Because $\mathcal{T} \gg 1$, the structure function evolves relatively slowly in these solutions, participating little in the faster Stokes-layer oscillations (which are better characterized by the shear stress or velocity; see the phase portrait also plotted in (c)). In other words, at these relaxation times, many cycles are required to evolve the microstructure away from the state that is almost frozen in by the initial condition.

When coupled with a large destruction parameter $\Gamma \gg 1$, long relaxation $\mathcal{T} \gg 1$ can also prompt persistent history dependence. In this limit, the structure function evolves according to

$$\Lambda_t \sim -\frac{\Gamma}{\mathcal{T}}|\dot{\gamma}|\Lambda. \tag{30}$$

That is, structure may be broken up by flow, but cannot recover owing to an excessive healing time. This extreme form of thixotropy (slow aging, but rapid destructuring) is thought to characterize a number of physical problems (*e.g.* [22]). In the corresponding Stokes problem, the continued attrition of the microstructure wherever fluid yields eventually reduces the rheology to constant viscosity ($\Lambda \to 0$ and $\tau \to \dot{\gamma} = u_y$); only where fluid remains unyielded can the microstructure survive. But because a plug invariably appears near the top free surface, and its extent depends on the stress history of the fluid, different solutions can emerge with varying plug thicknesses.

Such multiplicity is illustrated in Fig. 12, for three solutions with $(\Gamma, \mathcal{T}) \gg 1$ and different initial conditions ($\Lambda(y,0) = 0$, 0.79 and 1). Because both Γ and $\mathcal{T}$ are large but finite, the microstructure becomes severely compromised over the yielded regions, but is still able to heal over any persistent plugs. Consequently, the microstructure collapses over the lower part of the layer, but builds up to, or remains at, $\Lambda = 1$ within the overlying plug. The different initial conditions ensure that, over long times, the top structured plugs have different thicknesses in the three solutions. The varying plug thickness becomes reflected in the different lengths of the "stem" of the instantaneous $(\dot{\gamma}, \tau)$ relation along the τ−axes in Fig. 12(g-i). The two solutions shown in Fig. 11 also have plugs of different plug thickness (see panel (a)), although the difference is much less pronounced because Γ is smaller there.

The two-layer structure to the fluid implies that the lower part of the Stokes layer evolves nearly as a viscous fluid, with a top boundary condition set by an integral over the structured plug: *i.e.*

$$u_t = u_{yy}, \quad u(0,t) = -\cos t, \tag{31}$$

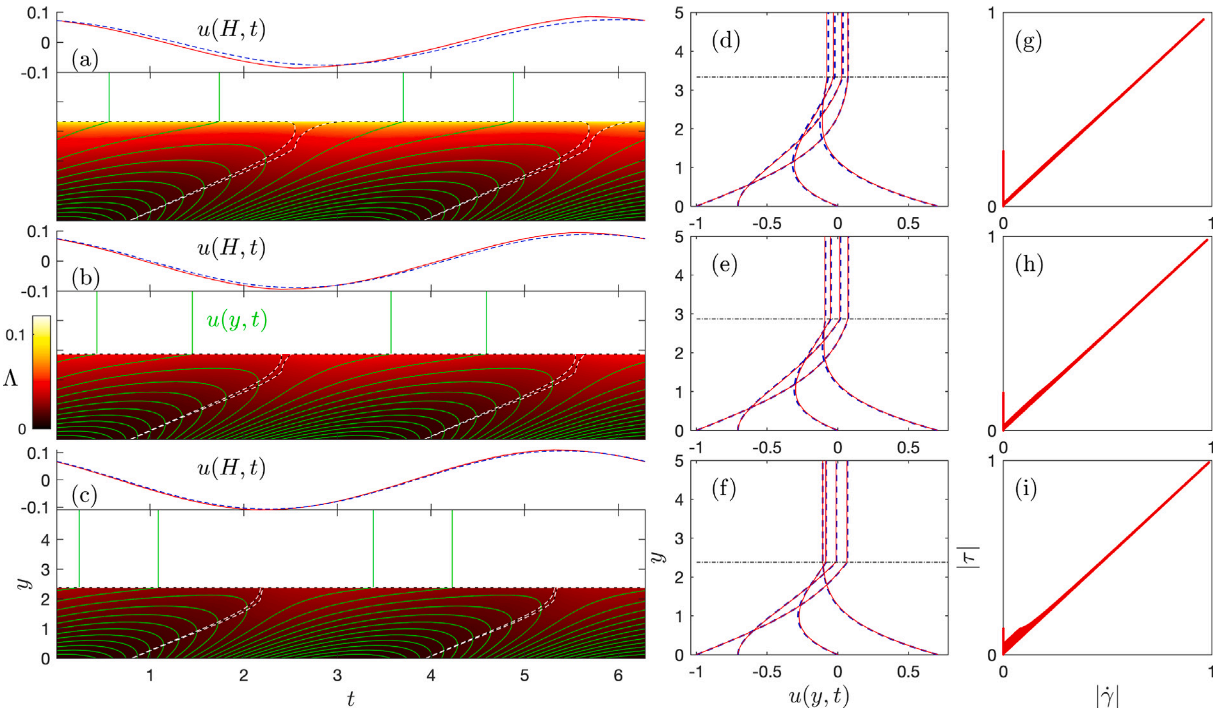

Fig. 12. Three thixotropic Stokes layers for $\Gamma = 200$, $\mathcal{T} = 100$, $H = 5$ and $\mathrm{Bi} = \frac{1}{2}$, computed from different initial conditions: (a,d,g) $\Lambda(y,0) = 0$, (b,e,h) $\Lambda(y,0) = 0.79$ and (c,f,i) $\Lambda(y,0) = 1$. (a)–(c) display time series of the surface speed $u(H,t)$ and density plots of the structure function $\Lambda(y,t)$, with superposed contours of constant speed $u(y,t)$ (green), and yield surfaces (black-and-white dashed lines). (d,e,f) show snapshots of $u(y,t)$ at four instants, with the dot-dashed horizontal lines denoting the yield surfaces $y = Y$. (g,h,i) display scatter plots of the solutions on the $(|\dot\gamma|, |\tau|)$–plane. The dashed lines in (a–f) show the predictions from (31)–(32), adopting values of Y taken from the numerical solutions.

and

$$(H - Y)u_t(Y,t) + u_y(Y,T) = 0, \tag{32}$$

where $y = Y$ denotes the yield surface. That level must be set independently, and is dictated by the interplay between rheological and dynamical evolution during an initial-value calculation from a specific initial condition. Analytical solutions to (31)–(32) are compared with numerical solutions to the full Stokes-layer problem in Fig. 12(a-f), after adopting values for Y taken from the latter.

5. Discontinuous shear thickening

To model a discontinuously shear thickening material, we employ a model based on that proposed by Wyart & Cates [12] and expanded upon by others [13–15]. The model combines an evolution equation for an order-parameter Λ,

$$\frac{\partial \Lambda}{\partial \tilde t} = \alpha|\dot{\tilde\gamma}|\left[\exp\left(-\frac{\tau_*}{|\tilde\tau|}\right) - \Lambda\right] + K\frac{\partial^2 \Lambda}{\partial \tilde y^2}, \tag{33}$$

with the viscosity law,

$$\mu(\Lambda) = \frac{\mu_0}{(\Lambda_o - \Lambda)^2}, \tag{34}$$

with parameters α, Λ_o and τ_*. In the model proposed by Wyart & Cates, the parameter Λ_o is determined with reference to three other parameters,

$$\Lambda_o = \frac{\phi_0 - \phi}{\phi_0 - \phi_1}, \tag{35}$$

where ϕ is the particle volume fraction and ϕ_0 and ϕ_1 are jamming fractions for suspensions of frictionless and frictional particles, respectively. The variable $\Lambda(y,t)$, satisfying $0 \le \Lambda \le \Lambda_o$, describes the fraction of frictional contacts, but for convenience and consistency with the previous section, we will continue to refer to Λ as a 'structure parameter'. The formulation is built on the idea that short-range repulsion keeps particles apart at low stress, maintaining a relatively low suspension viscosity. But frictional contact cannot be prevented at higher stresses $\tilde\tau$ and volume fractions ϕ. Instead, particles jam together to abruptly increase the viscosity.

Scaling using (4), we arrive at the dimensionless model,

$$\dot\gamma_t = \tau_{yy}, \qquad \tau = (\Lambda_o - \Lambda)^{-2}\dot\gamma,$$
$$\mathcal{T}\Lambda_t = |\dot\gamma|\left[\exp\left(-\frac{\Gamma}{|\tau|}\right) - \Lambda\right] + \beta\Lambda_{yy}, \tag{36}$$

where $\beta = K/(\alpha\mathcal{U}\mathcal{L})$, and

$$\mathcal{T} = \frac{\omega\mathcal{L}}{\mathcal{U}\alpha} \quad \& \quad \Gamma = \frac{\tau_*}{\rho\omega\mathcal{U}\mathcal{L}}, \tag{37}$$

play the role of a relaxation timescale and a dimensionless characteristic stress. Again, we assume that the upper surface is stress free ($\tau(y,t) = 0$; the no-slip case is briefly discussed in Appendix B) and no flux conditions apply ($\Lambda_y(0,t) = \Lambda_y(H,t) = 0$). We once more focus on the effect of rheological variations, and the impact of the parameters $\mathcal{T}$ and Γ, fixing $\beta = 10^{-6}$. We initialize the problem with $\dot\gamma(y,0) = 0$ and $\Lambda(y,0) = 0$, and again focus on the final periodic states.

In steady uniform shear, we find the flow curve,

$$\dot\gamma = \tau\left(\Lambda_o - e^{-\Gamma/|\tau|}\right)^2, \tag{38}$$

as illustrated in Fig. 13. The parameter Λ_o (equivalent to the solid fraction of the original model) controls whether the fluid thickens smoothly and continuously, like the redder curves in Fig. 13, or switches discontinuously because the steady-state flow curve bends back on itself at higher stress (bluer curves).

Sample numerical Stokes-layer solutions are shown in Figs. 14–16. In the first of these figures, a *continuously* shear thickening fluid is presented, with $\Lambda_o = 1.3 > 2e^{-\frac{1}{2}}$. For short relaxation times, the local fluid structure follows the steady flow curve (see panel (a)). Owing to the form of the constitutive model, the structure almost completely collapses during part of the cycle wherever stresses become sufficiently small. As $\mathcal{T}$ increases, however, the structure cannot fully relax and a time-dependent scatter plot of $(\dot\gamma, \tau)$ emerges with fluid remaining more

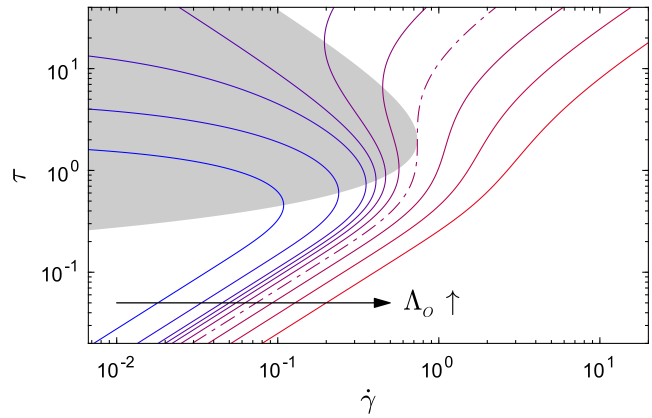

Fig. 13. Steady-state flow curves for $\Gamma = 1$ and $\Lambda_o = \{0.6, 0.82, 0.95, 1, 1.05, 1.12, 1.36, 1.6, 2\}$ (solid, from blue to red). The shaded region shows where the flow curve has negative slope and the dot-dashed curve with $\Lambda_o = 2\exp\left(-\frac{1}{2}\right)$ shows the critical case at which discontinuous thickening begins.

structured at the base of the layer (Fig. 14c,d). As with the thixotropic fluids, however, the surface speed is insensitive to these variations in Λ (Fig. 14b).

Solutions for *discontinuously* thickening fluids are shown in Fig. 15. In these examples, the structure functions develop a rich spatio-temporal pattern. For the case with higher $\mathcal{T}$ (panels (a,c)), the lengthier time required for relaxation exerts a stronger control on the dynamics, to the degree that the local $(\dot{\gamma}, \tau)$ scatter plot remains close to the steady-shear flow curve, even past its turn-around. For shorter relaxation times, however, uncontrolled shear thickening ensues (panels (b,d)), which builds up significant structure during brief periods of the cycle. This sudden thickening becomes reflected in abrupt jumps in surface speed.

For even lower relaxation times, the dynamics can become richer still, as illustrated in Fig. 16. In these examples, increasingly many events of abrupt shear thickening arise during the cycle as $\mathcal{T}$ is lowered. The surface speed reflects these events by developing a step-like signature. Multiple solutions even appear to be possible at the lowest relaxation times, characterized by different numbers of shear thickening events, as illustrated by the two solutions with $\mathcal{T} = 10^{-4}$ shown in Fig. 16 for different initial conditions. We have not traced in any detail how such multiple solutions come about or bifurcate from one another, and note only that the solutions are less straightforward to compute owing to the relatively short relaxation time.

6. Discussion

In this paper we have presented an analysis of the dynamics of Stokes layers of three different rheologically complex model fluids: a elasto-viscoplastic fluid, a thixotropic material, and a discontinuously shear-thickening fluid. For the first of these, we provided a more systematic exploration, allowing the layer to have either a free surface, or be bordered above by a stationary wall. When the layer is relatively thin, the latter upper boundary condition reproduces a simple, rheometric-type, oscillatory shear flow; the former allows for more novel dynamics by enabling thinner layers to plug up. When the layer is deeper, the spatio-temporal dynamics becomes rather richer than simple uniform shear for both boundary conditions. The novelties associated with a Stokes layer with a free surface led us to focus on that setting for the other two model fluids.

A theory for viscoplastic Stokes layers was presented previously by Balmforth et al. [2], partly with the aim of examining what rheological inferences might be made by harnessing such flows. Indeed, a main goal of that work was to compare theoretical predictions with observations from experiments with layers of kaolin slurry in a motorized tray. The comparison had mixed successes: whilst the onset of relative surface motion coincided with the predicted threshold, $H = \mathrm{Bi}$ or $\rho\omega\mathcal{H}\mathcal{V} = \tau_p$, the amplitude of the fluid motions showed discrepancies. Some quick calculations based on the degree of elastic deformation of the slurries recorded rheometrically suggested at the time that elasticity was unlikely to be responsible for this disagreement. Instead, it was suggested that the thixotropic nature of kaolin slurries was the culprit.

The experiments reported in [2] were conducted with different slurries, depths, forcing frequencies and tray speeds, implying a spectrum of different values for the dimensionless groups of the problem. In addition, the steady-shear flow curves found for the kaolin slurries (from cone-and-plate rheometry) suggested convenient Herschel–Bulkley fits with a power-law index of $n \approx \frac{1}{3}$ (in contrast to the Bingham law to which our elasto-viscoplastic model limits for $\mathrm{De} = 0$). The current theory is therefore not matched to these experiments. To bring our analysis closer, we may make use of the Herschel–Bulkley generalization of the elasto-viscoplastic model proposed in [23]. With this generalization, the factor $\max(0, |\tau| - \mathrm{Bi})$ in the evolution equations in (14) becomes raised to the power n^{-1}. The Stokes length must also now be defined by

$$\mathcal{L} = \left(\frac{K\mathcal{V}^{n-1}}{\rho\omega}\right)^{\frac{1}{n+1}}, \tag{39}$$

where $\mu_o = K(\mathcal{V}/\mathcal{L})^{n-1}$ is an effective viscosity (beware of a typo in the corresponding formula provided in [2]). Finally, Balmforth et al. quote an elastic (Young's) modulus of $E = 10^4$ Pa for the kaolin slurries, suggesting a characteristic relaxation rate $\lambda = E/\mu_o$ for use in the Deborah number of the elasto-viscoplastic model.

A selection of the data taken from [2] are plotted in Fig. 17. The first three panels display the range of estimated values for the dimensionless parameters, H, Bi and De. Measurements of the maximum relative surface speed are then plotted in Fig. 17(d,e) against H/Bi. In the first of these plots, the symbols are coloured according to Bingham number; for the second plot, the symbols are coloured by De. Included in Fig. 17(d) are theoretical predictions of the revised model, assuming relatively a small elasticity parameter ($\mathrm{De} = 10^{-4}$ and $\beta = 0$), and taking $n = \frac{1}{3}$ and $\mathrm{Bi} = \frac{1}{2}$, 1 or 2 (which punctuate the range seen in Fig. 17(b)). As concluded by Balmforth et al. [2], the threshold for relative motion is somewhat well predicted by $H/\mathrm{Bi} = 1$, but the predicted trends with varying Bi without elasticity cannot reproduce the experimental observations. Instead, in Fig. 17(e), we include theoretical results that incorporate elasticity, for Deborah numbers that appear to be typical of the experimental range (and taking $\mathrm{Bi} = 1$, $n = \frac{1}{3}$ amd $\beta = 0$). The elevated response of surface velocity due to elastic recoil in these theoretical predictions certainly seems capable of rationalizing the experimental observations, even though parameters have not been carefully matched.

Similar conclusions were reached by Lacaze et al. [11], who conducted experiments with a Carbopol suspension contained in the annular gap between two cylinders, driving motion by the oscillatory rotation of the inner cylinder. They found that the observed motions could be explained by a similar theory to that discussed in §3. Prominent in both the modelling by [11] and the current work is the impact of elastic deformation below the yield stress, which can become especially significantly if the Stokes-layer oscillations resonate with elastic waves. Indeed, we have seen that one can resonantly drive elastic waves to high amplitudes and yield, even if the plastic yield condition $H > \mathrm{Bi}$ is not met (cf. Fig. 4). In other words, elasticity can significantly impact the behaviour of viscoplastic fluids even in situations where a basic scaling estimate suggests its impact should be weak, predominantly owing to this sub-yield-stress elastic deformation. Overall, the surface speed provides a useful diagnostic of rheology for Stokes layers of elasto-viscoplastic fluids with a free surface.

By contrast, and counter to the conclusions reached in [2], it looks more challenging to explain the experimental results in Fig. 17 using

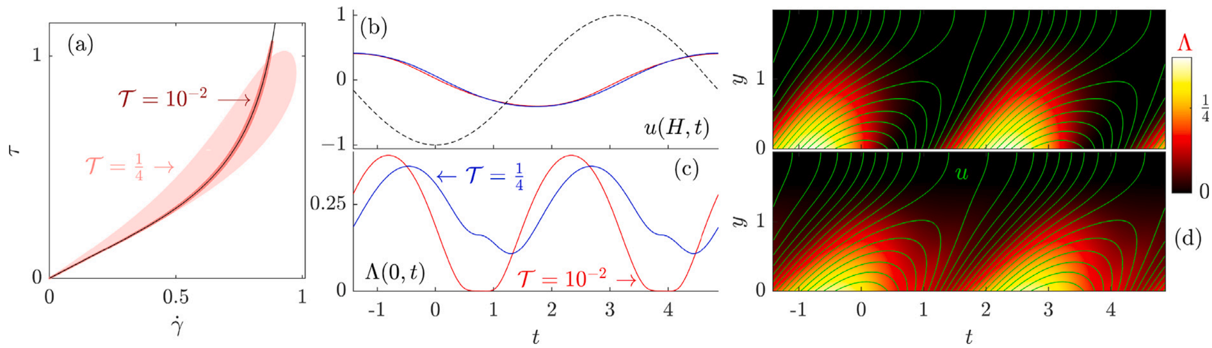

Fig. 14. Steady-state periodic solutions for $(\Lambda_o, \Gamma, H) = (1.3, 1, 2)$ and the two relaxation times $\mathcal{T} = 0.01$ and $\frac{1}{4}$. In (a), the flow curve (solid line) is compared with scatter plots of $(\dot{\gamma}, \tau)$ (darker dots: $\mathcal{T} = 0.01$; lighter dots: $\frac{1}{4}$). Time series of the surface speed $u(H,t)$ and basal structure function $\Lambda(0,t)$ are plotted in (b,c). Density maps of $\Lambda(y,t)$ with superposed contours of constant $u(y,t)$ (green) are shown in (d), with the solution for $\mathcal{T} = 0.01$ shown in the top panel and that for $\frac{1}{4}$ in the bottom panel.

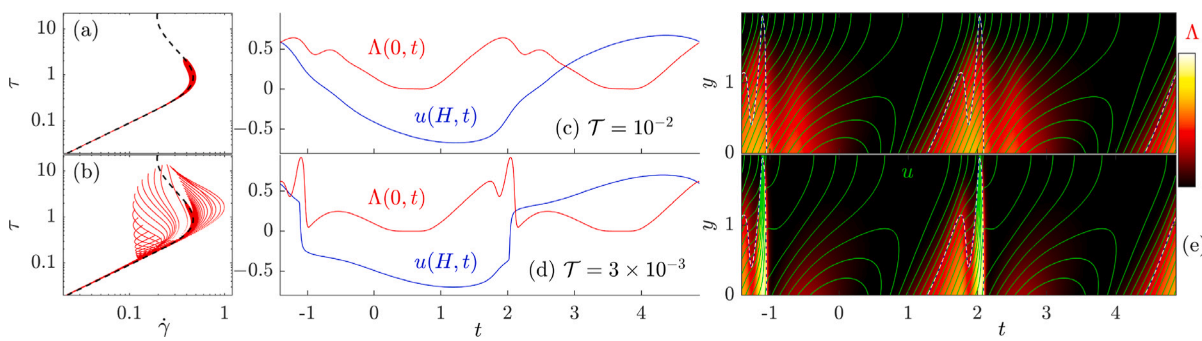

Fig. 15. Steady-state periodic solutions for (a,c) $\mathcal{T} = 10^{-2}$ and (b,d) $\mathcal{T} = 3 \times 10^{-3}$, with $(\Lambda_o, \Gamma, H) = (1.05, 1, 2)$. Flow curves (dashed) are compared with scatter plots of $(\dot{\gamma}, \tau)$ in (a,b). Time series of $u(H,t)$ and $\Lambda(0,t)$ are shown in (c,d). Density maps of $\Lambda(y,t)$ with superposed contours of constant $u(y,t)$ (green) are shown in (e) (top panel: $\mathcal{T} = 10^{-2}$; bottom panel: $\mathcal{T} = 3 \times 10^{-3}$). The dashed contours indicate where τ reaches the turn-around of the flow curve.

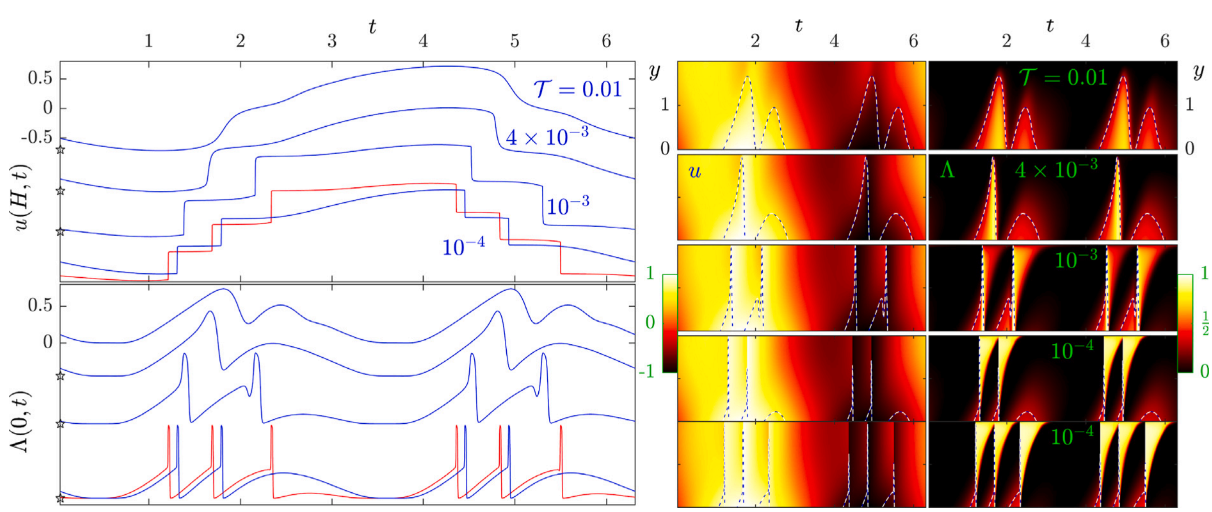

Fig. 16. Steady-state periodic solutions for varying $\mathcal{T}$ (as indicated) with $(\Lambda_o, \Gamma, H) = (1, 1, 2)$. Two solutions are shown for $\mathcal{T} = 10^{-4}$: the case shown in blue has initial condition $\Lambda(y, 0) = 0$; the case plotted in red uses an initial condition given by the final solution with $\mathcal{T} = 10^{-3}$. Time series of $u(H,t)$ and $\Lambda(0,t)$ are plotted in the main panels on the left (with the solutions for lower $\mathcal{T}$ offset for clarity; the stars on the y–axes indicate the offsets); the corresponding density maps of $u(y,t)$ and $\Lambda(y,t)$ are shown on the right. Dashed contours again indicate where τ reaches the turn-around of the flow curve.

the version of our model that incorporates thixotropy: in none of the solutions of that model variant does the maximum relative surface speed significantly exceed that of the wall (*i.e.* $\max(u|_{y=H} + \cos t) > 1$). Indeed, as we have seen, the imprint of thixotropic rheology on surface flow speeds is relatively weak, and the fluid response looks much like that for an ideal viscoplastic fluid with a suitably defined yield stress. Nevertheless, thixotropic viscosity bifurcations, should they occur, are not inconsequential because they prompt internal layering between structured or destructured fluid. Moreover, many cycles of the Stokes layer may be needed for structure to adjust if relaxation times are long, and when the healing of the microstructure becomes too slow, the thicknesses of fully structured regions can depend sensitively on the history of flow.

As a counterpoint to the Stokes layer of fluids with a yield stress, we have also briefly explored the dynamics of Stokes layers of discontinuously shear thickening fluid. With such material, Stokes-layer oscillations can prompt abrupt thickening events that introduce sudden

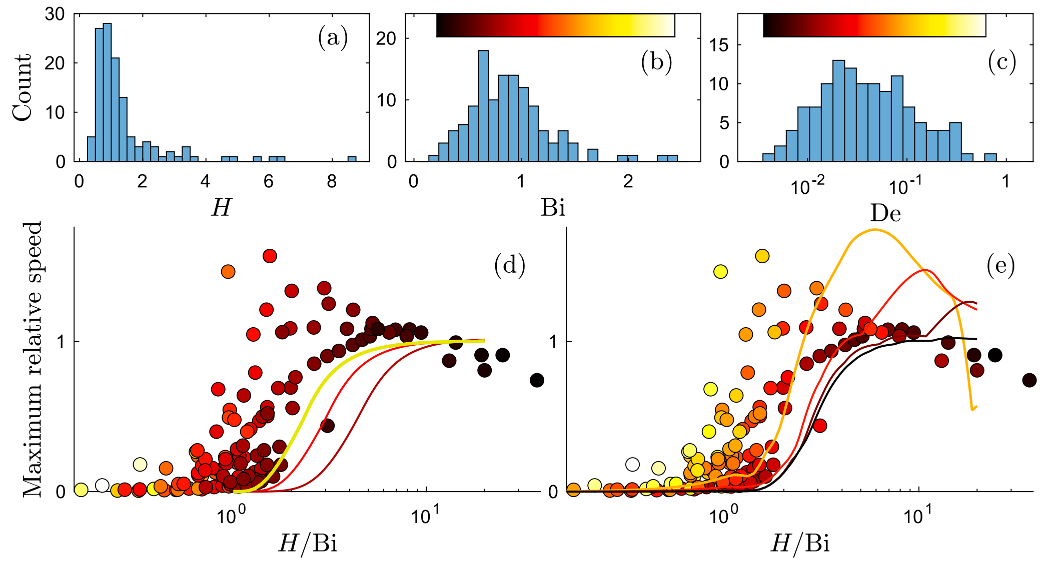

Fig. 17. Experimental results from [2]. These tests were performed using kaolin slurries of different depths in a tray moving at different speeds and frequencies. The range of the resulting values for H, Bi and De are shown in (a), (b) and (c). The maximum relative surface motion (*i.e.* $\max(u_{y=H}+\cos t)$) recorded in all the experiments is plotted in (d,e). For (d), the points are coloured according to the Bingham number (the colour scale is shown in (b)), and theoretical curves for $\mathrm{De}=10^{-4}$ and $\mathrm{Bi}=\frac{1}{2}$, 1 and 2 are plotted as the solid lines (all with $n=\frac{1}{3}$ and $\beta=0$). For (e), the points are coloured according to De (see (c)), and the solid lines show theoretical curves for $\mathrm{De}=0.00316$, 0.01, 0.0316 and 0.1 (with $\mathrm{Bi}=1$, $n=\frac{1}{3}$ and $\beta=0$).

jumps in surface speed. In other words, fluid rheology becomes more obviously encoded into the surface-speed signal.

We close by noting that we have assumed that the flow always remains one-dimensional and never develops spatial structure in the direction of flow. In fact, such one-dimensional motion may well suffer instabilities to spatially varying perturbations in the flow direction, as seen in rheometers or rheometric flows [24–27]. We leave such possibilities, and any two-dimensional stability theory of the one-dimensional base states that we have presented, to future work.

CRediT authorship contribution statement

D.R. Hewitt: Writing – review & editing, Writing – original draft, Formal analysis. **N.J. Balmforth:** Writing – original draft, Formal analysis.

Declaration of competing interest

The authors declare that they have no known competing financial interests or personal relationships that could have appeared to influence the work reported in this paper.

Data availability

Data will be made available on request.

Acknowledgements

NJB thanks the Isaac Newton Institute for Mathematical Sciences, Cambridge, for support and hospitality during the programme *Anti-diffusive dynamics: from sub-cellular to astrophysical scales* where work on this paper was undertaken. This work was supported by EPSRC, United Kingdom grant no EP/K032208/1.

Appendix A. Numerical details

To solve the various model equations numerically, we replace partial derivatives in space with centred finite differences on a uniform grid of 1000 or more points. The resulting set of ordinary differential equations are then solved as an initial-value problem using the solver DASSL [28]. To ease each computation, we smooth out the switches present in each system: for the purely viscoplastic model (Eq. (14) with $\mathrm{De}=0$), we eliminate $\dot\gamma(y,t)$ and write $\tau_t\Theta(|\tau|-\mathrm{Bi})=\tau_{yy}$, then replace the step function by

$$\Theta(|\tau|-\mathrm{Bi})\to\frac{1}{2}\left[1+\frac{\tau^2-\mathrm{Bi}^2}{\sqrt{(\tau^2-\mathrm{Bi}^2)^2+\varepsilon^2}}\right], \tag{A.1}$$

where the regularization parameter ε is taken to be 10^{-4} or less. With $\mathrm{De}>0$, we use no regularization and solve (14) directly. For the thixotropic model, we solve (24) with the replacements $|\dot\gamma|\to\sqrt{\varepsilon_1^2+\dot\gamma^2}$ and $\mu\to\Lambda_o/[(1-\Lambda)\ \max(\varepsilon_2,\Lambda_o-\Lambda)]$, taking $\varepsilon_1=\varepsilon_2=10^{-8}$. Finally, for the discontinuous shear thickening model, we replace $|\tau|$ and $|\dot\gamma|$ with $\sqrt{\tau^2+\varepsilon^2}$ and $\sqrt{\dot\gamma^2+\varepsilon^2}$ (respectively), with $\varepsilon=10^{-4}$.

For the latter two models, we adopt values for β that are relatively small. In all cases, the adequacy of spatial resolution was confirmed by performing more computations with different numbers of grid points and varying β. For no cases did the value of β, and microstructural diffusion, play a significant role.

Appendix B. No-slip Stokes layers

For a comparison of thixotropic Stokes layers with either a free or no-slip top surface, we show solutions in Fig. B.18 equivalent to those in Figs. 8 and 9 of the main text. The no-slip solutions in Fig. B.18 differ mainly in how the shear stress over the upper part of the layer is no longer demanded to become small and fluid here therefore remains sheared. As a consequence, structure cannot build up against the top surface to the degree that it does with free slip. Similarly, when the relaxation time becomes long, the spatial variation of the time-independent profile of the structure function remains relatively weak. Aside from such details, the dynamics of thixotropic Stokes

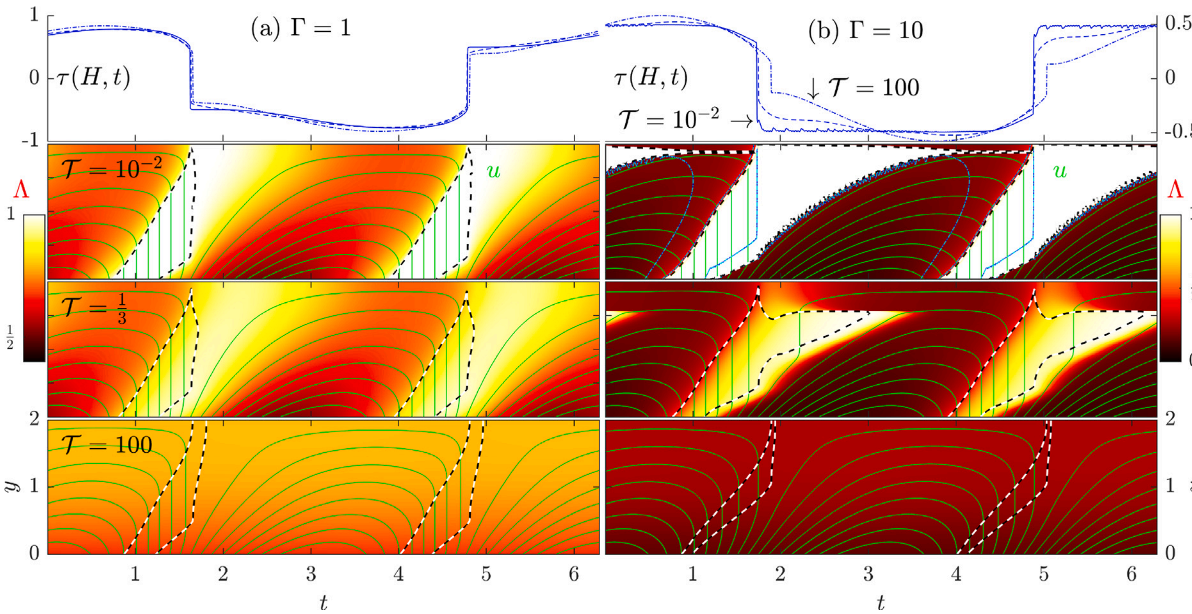

Fig. B.18. Thixotropic Stokes layers with a no-slip top surface for (a) $\Gamma = 1$ (corresponding to the free-surface solutions in Fig. 8) and (b) $\Gamma = 10$ (corresponding to solutions in Fig. 9). The top panels show the surface shear stress $\tau(H,t)$; the space–time density plots below display $\Lambda(y,t)$ along with superposed contours of constant speed (solid green) and the yield surfaces (black-and-white dashed). In each case, solutions with $\mathcal{T} = 10^{-2}$, $\frac{1}{3}$ and 100 are displayed (solid, dashed and dot-dashed, respectively, in the top panels). For the solution with $(\Gamma, \mathcal{T}) = (10, 10^{-2})$, the additional speckled contours indicate the stress contours $\tau = \tau_{_\Lambda}$ and $\tau = \tau_c$.

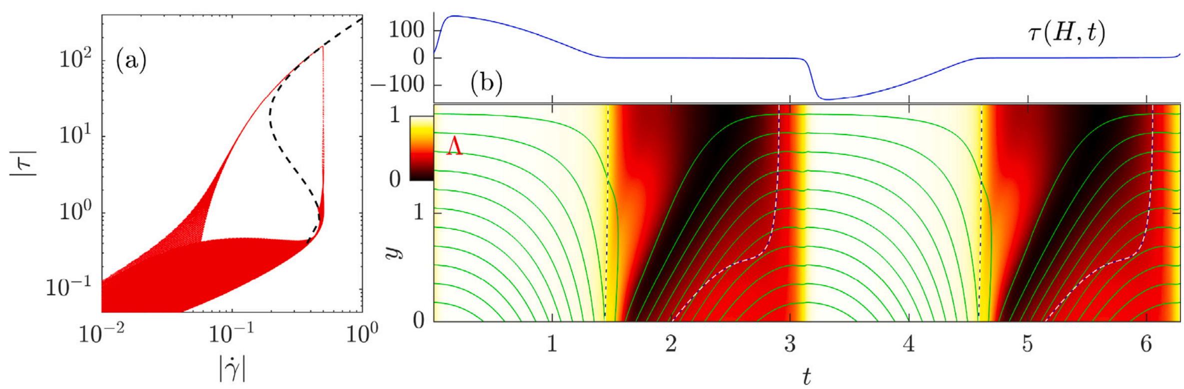

Fig. B.19. A discontinuous shear-thickening Stokes layer with a no-slip top surface for $(\mathcal{T}, \Lambda_o, \Gamma, H) = (10^{-2}, 1.05, 1, 2)$ (corresponding to the free-surface solution in Fig. 15(a)). In (a), the flow curve (dashed line) is compared with scatter plots of $(\dot{\gamma}, \tau)$. Panel (b) displays a time series of $\tau(H,t)$ and a density map of $\Lambda(y,t)$, with superposed contours of constant $u(y,t)$ (green) The dashed contour indicates where τ reaches the turn-around of the flow curve.

layers with a no-slip top surface largely follows that of layers with a free surface. Although the space–time pattern of the solutions for Λ remains somewhat complicated for sufficiently low relaxation time $\mathcal{T}$ in Fig. B.18, the corresponding patterns of the stress are again not so different from their Bingham counterpart (in Fig. 1(b), for De $= 0$).

A Stokes-layer solution with a no-slip top surface for the discontinuous shear-thickening model of §5 is presented in Fig. B.19, which corresponds to the free-surface solution shown in Fig. 15(a). Because the shear stress is again no longer forced to become small over the upper part of the layer, the dynamics in this case is more similar to that of a controlled-shear-rate rheometer. Consequently, when the relaxation time is small, the local stress-shear-rate relation attempts to follow the stable branches of the S-shaped flow curve. Sudden stress jumps then emerge at the turn-arounds of the flow curve, corresponding to abrupt shear-thickening events that span the fluid layer. As a result, stress signals take the form of large-amplitude relaxation oscillations. Note that the upper branch of the S-shaped flow curve is relatively uncertain in discontinuously shear-thickening rheological models (*cf.* [15]). Stokes-layer studies might therefore help to shed some light on how reliable these models might be.

References

[1] J. Ortín, Stokes layers in oscillatory flows of viscoelastic fluids, Phil. Trans. R. Soc. A 378 (2174) (2020) 20190521.
[2] N.J. Balmforth, Y. Forterre, O. Pouliquen, The viscoplastic Stokes layer, J. Non-Newton. Fluid Mech. 158 (1–3) (2009) 46–53.
[3] P.A. Vasquez, Y. Jin, K. Vuong, D.B. Hill, M.G. Forest, A new twist on stokes' second problem: Partial penetration of nonlinearity in sheared viscoelastic layers, J. Non-Newton. Fluid Mech. 196 (2013) 36–50.
[4] C.R. McArdle, D. Pritchard, S.K. Wilson, The stokes boundary layer for a thixotropic or antithixotropic fluid, J. Non-Newton. Fluid Mech. 185 (2012) 18–38.
[5] E.M. Hinton, J.F. Collis, J.E. Sader, The motion of a layer of yield-stress material on an oscillating plate, J. Fluid Mech. 959 (2023).
[6] P. Saramito, A new constitutive equation for elastoviscoplastic fluid flows, J. Non-Newton. Fluid Mech. 145 (1) (2007) 1–14.
[7] R.G. Larson, Y. Wei, A review of thixotropy and its rheological modeling, J. Rheol. 63 (3) (2019) 477–501.
[8] J.F. Morris, Shear thickening of concentrated suspensions: Recent developments and relation to other phenomena, Annu. Rev. Fluid Mech. 52 (2020) 121–144.
[9] Y.S. Park, P.L. Liu, Oscillatory pipe flows of a yield-stress fluid, J. Fluid Mech. 658 (2010) 211.
[10] J. Stickel, J. Knutsen, M. Liberatore, Response of elastoviscoplastic materials to large amplitude oscillatory shear flow in the parallel-plate and cylindrical-couette geometries, J. Rheol. 57 (6) (2013) 1569–1596.

[11] L. Lacaze, A. Filella, O. Thual, Steady and unsteady shear flows of a viscoplastic fluid in a cylindrical couette cell, J. Non-Newton. Fluid Mech. 220 (2015) 126–136.

[12] M. Wyart, M.E. Cates, Discontinuous shear thickening without inertia in dense non-brownian suspensions, Phys. Rev. Lett. 112 (9) (2014) 098302.

[13] R.N. Chacko, R. Mari, M.E. Cates, S.M. Fielding, Dynamic vorticity banding in discontinuously shear thickening suspensions, Phys. Rev. Lett. 121 (10) (2018) 108003.

[14] J. Richards, J. Royer, B. Liebchen, B. Guy, W. Poon, Competing timescales lead to oscillations in shear-thickening suspensions, Phys. Rev. Lett. 123 (3) (2019) 038004.

[15] B. Darbois Texier, H. Lhuissier, B. Metzger, Y. Forterre, Shear-thickening suspensions down inclines: from kapitza to oobleck waves, J. Fluid Mech. 959 (2023) A27.

[16] H.A. Barnes, Thixotropy—a review, J. Non-Newton. Fluid Mech. 70 (1–2) (1997) 1–33.

[17] J. Mewis, N.J. Wagner, Thixotropy, Adv. Colloid Interface Sci. 147 (2009) 214–227.

[18] P. Coussot, Q.D. Nguyen, H. Huynh, D. Bonn, Viscosity bifurcation in thixotropic, yielding fluids, J. Rheol. 46 (3) (2002) 573–589.

[19] K. Dullaert, J. Mewis, A structural kinetics model for thixotropy, J. Non-Newton. Fluid Mech. 139 (1–2) (2006) 21–30.

[20] P.C. Møller, J. Mewis, D. Bonn, Yield stress and thixotropy: on the difficulty of measuring yield stresses in practice, Soft Matter 2 (4) (2006) 274–283.

[21] A.N. Alexandrou, N. Constantinou, G. Georgiou, Shear rejuvenation, aging and shear banding in yield stress fluids, J. Non-Newton. Fluid Mech. 158 (1–3) (2009) 6–17.

[22] P. Coussot, Q.D. Nguyen, H.T. Huynh, D. Bonn, Avalanche behaviour in yield stress fluids, Phys. Rev. Lett. 88 (2002) 175501.

[23] P. Saramito, A new elastoviscoplastic model based on the herschel–bulkley viscoplastic model, J. Non-Newton. Fluid Mech. 158 (1–3) (2009) 154–161.

[24] J.K. Dhont, W.J. Briels, Gradient and vorticity banding, Rheol. Acta 47 (2008) 257–281.

[25] G. Ovarlez, A. Vu Nguyen Le, W.J. Smit, A. Fall, R. Mari, G. Chatté, A. Colin, Density waves in shear-thickening suspensions, Sci. Adv. 6 (16) (2020) eaay5589.

[26] R.J. Hommel, M.D. Graham, Flow instabilities in circular couette flow of wormlike micelle solutions with a reentrant flow curve, J. Non-Newton. Fluid Mech. 324 (2024) 105183.

[27] V. Rathee, J. Miller, D.L. Blair, J.S. Urbach, Structure of propagating high-stress fronts in a shear-thickening suspension, Proc. Natl. Acad. Sci. 119 (32) (2022) e2203795119.

[28] L. Petzold, Dassl. A Differential/Algebraic System Solver, Tech. Rep., Lawrence Livermore National Lab.(LLNL), Livermore, CA (United States), 1982.